

JCTC

Journal of Chemical Theory and Computation

Search and Characterization of Transition State Structures in Crystalline Systems Using Valence Coordinates

Albert Rimola,[†] Claudio Marcelo Zicovich-Wilson,^{*,‡} Roberto Dovesi,[†] and Piero Ugliengo^{*,†}

Dipartimento Chimica IFM, NIS Centre of Excellence and INSTM (Materials Science and Technology) National Consortium, University of Torino, Via P. Giuria 7, 10125 Torino, Italy, and Facultad de Ciencias, Universidad Autónoma del Estado de Morelos, Av. Universidad 1001, Col. Chamilpa, 62209 Cuernavaca, Morelos, Mexico

Received December 19, 2009

Abstract: Several tools that allow molecules, polymers, slabs, and crystals to be optimized in valence coordinates as well as a suitable saddle point optimization technique to search for transition state structures for this kind of system have been implemented in the *ab initio* periodic CRYSTAL code. The adoption of these localized coordinate systems largely facilitates the study of chemical processes in periodic systems with atomic connectivity, as occurs in catalytic reactions on zeolites, clathrates, or oxidic surfaces. As a paradigmatic case, the new features have been illustrated to study the proton jump between oxygen atoms of the Brønsted site in the H-chabazite zeolite. The electronic and Gibbs free energy profiles of the most representative proton jump channels have been computed at the B3LYP level, both for a dry H-chabazite as well as in the presence of one H₂O molecule acting as a proton transfer helper. Because of the accuracy allowed by the optimization technique, all stationary points located have been characterized as minima or saddle points by computing the harmonic frequencies and checking, for the latter, that the corresponding transition eigenvectors were in agreement with the selected reaction path. The remarkable agreement between the results with both theoretical and experimental literature data gives credit to the accuracy and robustness of the present implementations in the CRYSTAL code.

1. Introduction

The study and characterization of transition state (TS) structures by computational methods is the key step to understanding chemical reactivity. When simulating homogeneous/heterogeneous catalytic processes, it is of paramount relevance to assess the bounty of hypothetical catalysts and to improve their performance through the characterization and design of the activated complexes at the atomic level. Albeit TS optimizations can in principle be performed by means of similar computational strategies of those adopted for minimizations,^{1–3} in practice, the former has never become an entirely routine process as it is for the latter. The

remarkable difference between both kinds of optimization relies on the quasi-quadratic behavior of the respective optimum domains on the potential energy surface (PES), i.e., while for minima the quadratic basin is large enough to successfully locate a minimum from a wide variety of starting structures, in the TS structures, the basin around a saddle point is much reduced, so that a very good initial guess is required to ensure the convergence through the desired TS by the adopted algorithm. In some way, properly guessing a good starting point still requires a good deal of chemical ingenuity, although several techniques have been proposed to largely help this task.^{2,4–9}

The choice of a suitable coordinate system to describe the structures may significantly improve the search of saddle points by enlarging the TS quadratic domains. In molecular cases, a recurrent strategy is based on the use of internal valence coordinates, usually built through Z-matrix or

* Corresponding author e-mail: piero.ugliengo@unito.it (P.U.); claudio@uaem.mx (C.M.Z.-W.).

[†] University of Torino.

[‡] Universidad Autónoma del Estado de Morelos.

redundant schemes.^{1,3} The localized character of these coordinate systems enables a proper description of most of the chemical reactions, involving bond breaking/making processes. This coordinate system, additionally, facilitates a reasonably fast convergence of the optimization technique and permits one to devise straightforward strategies to guess starting structures for the TS optimization.

In periodic calculations, other strategies are customarily preferred to locate TS structures. The most widely used is the so-called climbing image-nudged elastic band (CI-NEB).¹⁰ In this method, the saddle point optimization is substituted by the energy minimization of a supersystem consisting of a set of “images” that sample a path connecting reactants and products which are linked to each other by a kind of “spring forces”. The resulting images define the minimum energy path (MEP) of the reaction, the image corresponding to the highest energy being considered the TS. This technique, thus, somehow neglects the localized character of the chemical reactions. The most appealing feature of the CI-NEB method relies on the fact that a suitable starting point for the TS optimization is, in practice, not mandatory, as only the optimized reactant/product structures and the total number of images along the path are needed. Also, the minimization process is, in general, quite stable. However, as a drawback of the method, the nonquadratic character of the overall function considered in the global optimization often slows down the convergence. This is reflected in the known fact that the steepest descent method adopted for the CI-NEB optimization¹¹ provides directions toward the minima which are far from being conjugate, hence causing slow convergence.¹² In addition, for most periodic codes, the CI-NEB implementation does not allow cell deformations along the MEP because of the complication in the definition of spring forces for lattice vectors. Although extensions of the method have been recently formulated to include cell deformations in the path,^{11,13,14} to our knowledge, they have still not been implemented in standard *ab initio* periodic codes.

Other limitations of the bare CI-NEB arise from the coordinate system adopted to define the structure of the images. While for molecular cases the method works unambiguously with Cartesian coordinate systems defined, for each image, on their corresponding center of mass, for periodic systems this is meaningless, as the coordinate system needs to be centered on arbitrary points for each image. Accordingly, depending on this choice, different sets of images can be generated for the same system. For solid state reactions involving bond breaking/making of structures with complex connectivity (as the case of zeolites), the PES defined on the Cartesian coordinates base exhibits complicated shapes which hamper a fast convergence of the CI-NEB method. This may be the reason why the CI-NEB method is rarely used to search for TS in 3D periodic systems, whereas it has been the method of election for studying reactions occurring on 2D surfaces where the above complications are usually absent.

Because of the enormous relevance of heterogeneous catalysis for the modern society, it is even more important to implement the efficient location of TS in the solid state

context, the surfaces of many crystals being the places where the catalytically active sites reach their maximum activity.¹⁵ It is worth mentioning that the focuses are not only on the “classical” flat surfaces of compact solids but are also on the internal curved walls of microporous materials like zeolites and metal organic frameworks.¹⁶

In the present work, we show that the adoption of a system of valence coordinates is not only useful for locating TS in molecules but also in periodic systems with complex connectivity to simplify the study of reaction paths. As shown in what follows, the coordinate system considered here is constituted by a set of redundant internal valence (RIV) coordinates generated according to previous prescriptions on molecular^{1,3} and crystalline¹⁷ systems. The adoption of these coordinate systems allows one to consider very straightforward methods for the location of the TS, such as the so-called distinguished reaction coordinate (DRC) one,¹⁸ which is still one of the most used for molecular systems, at least when dealing with few coordinates that dominate the reaction path. In the simplest version of DRC, one degree of freedom, called the distinguished coordinate, is chosen and kept fixed at a sequence of values that are representative of the reaction path, while all the other coordinates are relaxed for each of these values. The maximum-energy geometry along the path is taken as the initial guess for the saddle-point search. Here, the localization of the saddle point requires the calculation of the Hessian matrix of the starting structure. A developing version of the CRYSTAL code¹⁹ is here employed in which the automatic mono- and bidimensional scan along valence coordinates has been implemented.

As anticipated, the behavior of acidic zeolites is of paramount importance because of their central role as catalysts in a large number of key industrial organic transformations.^{20–23} The so-called bridging hydroxyl groups belonging to the “Si–O(H)–Al” Brønsted acidic sites exhibit a rather strong acidic proton, as it is well-known that molecules adsorbed in the zeolite cages can easily become protonated in proximity of these acidic sites.²⁴ Indeed, because proton transfer reactions are key steps in heterogeneously acid-catalyzed reactions, the bridging hydroxyl groups are considered as true catalytic sites. In addition, the mobility of these protons is also important for ion transport in electrolytes, whose potential applications have recently been revealed with the fine-tuning of zeolite-based microfuel cells.²⁵ In the present work, to focus on a paradigmatic case but relevant from the catalytic point of view, the proton jumps occurring in the acidic chabazite, both in dry conditions and in the presence of one water molecule, have been dealt with. By applying the DRC technique facilitated by describing the problem in RIV coordinates, all the relevant saddle points have been located and characterized by computing both the electronic and free energy barriers of the proton motions. It is worth mentioning that the present implementation allows full relaxation of the cell parameters together with the atomic positions both in the search of the TS domain and in the saddle point optimization. Along this line, it is worth noting that disregarding cell relaxation may (i) introduce some artifacts in the estimation of the reaction energy barriers for localized chemical processes and (ii)

hinder the accurate characterization of bulk phase transitions. Both of these facts do highlight the usefulness of the present approach in the study of reactivity in 3D periodic systems.

2. Methods

2.1. Computational Details. All periodic calculations were carried out with a development version of the ab initio code CRYSTAL06.¹⁹ This code describes the many-electron wave function as a linear combination of crystalline orbitals, which, in turn, are expanded in terms of Gaussian-type functions (GTF), thus allowing one to treat molecules, 1D polymers, 2D surfaces (slabs), and 3D crystals (bulks) with the same level of accuracy.

Both Hartree–Fock (HF), pure PBE²⁶ and PW91²⁷ exchange-correlation density functionals (DF), as well as the hybrid PBE0²⁸ and B3LYP^{29,30} DF methods have been used for calculations of the present work with Gaussian basis sets of polarized double- ζ quality. Details of the adopted GTF basis set are available on the CRYSTAL Web site.³¹ Here, for the sake of brevity, only the exponents of the outer shells (in Bohr⁻²) are explicitly given: H, 31G* ($\alpha_s = 0.161$, $\alpha_p = 1.1$); O, 6-31G* ($\alpha_{sp} = 0.27$, $\alpha_d = 0.8$); Si, 66-21G* ($\alpha_{sp} = 0.13$, $\alpha_d = 0.5$); Al, 88-31G* ($\alpha_{sp} = 0.28$, $\alpha_d = 0.47$). To improve the accuracy, some calculations with a polarized triple- ζ basis set for the atoms of H (311G*, $\alpha_s = 0.10$ and $\alpha_p = 0.75$), O (6-311G*, $\alpha_{sp} = 0.26$ and $\alpha_d = 0.13$), and Si (88-31G*, $\alpha_{sp} = 0.193$, $\alpha_d = 0.61$) have been also carried out.

The Hamiltonian matrix has been diagonalized in 14 reciprocal lattice points (k -points), corresponding to a shrinking factor of 3.³² Tolerances of 10^{-6} and 10^{-14} were used for the Coulomb and exchange series, respectively.³² The DFT exchange-correlation contribution is integrated numerically on a grid of points. Radial and angular points of the atomic grid are generated through Gauss-Legendre and Lebedev quadrature schemes. A pruned grid consisting of 75 radial points and a variable number of angular points, with a maximum of 974 angular points in the most accurate integration region (usually named (75, 974)p), has been used.^{33,34} The condition for the SCF convergence was set to 10^{-8} and 10^{-11} Hartree for minima and saddle points, respectively, on the energy difference between two subsequent cycles.

A full relaxation of both lattice parameters and atomic coordinates of the H-chabazite was performed within the $P1$ symmetry. The geometry optimization for minima was performed by means of a quasi-Newton algorithm in which the quadratic step (BFGS Hessian updating scheme) is combined with a linear one (parabolic fit), as proposed by Schlegel.³⁵ As concerns the TS optimizations, they are performed adopting the method usually referred to as “Eigenvector following” proposed by Simons and Nichols,³⁶ and the Hessian update has been performed by combining the BFGS and the Murtagh-Sargent approaches³⁷ in the manner proposed by Bofill.³⁸ Convergence was tested on the root-mean square (RMS) and the absolute value of the largest component of the gradients and the estimated displacements. The threshold for the maximum force, the

RMS force, the maximum atomic displacement, and the RMS atomic displacement on all atoms were set to 0.00045, 0.00030, 0.00180, and 0.00120 au, respectively. By using the same strategy first adopted in Gaussian 80,³⁹ optimizations were considered complete when the four above conditions were simultaneously satisfied (see ref 40 for specific details on the CRYSTAL06 implementation).

Phonon frequencies of the considered systems have been calculated as the eigenvalues obtained by diagonalizing the mass-weighted Hessian matrix at Γ point (point $k = 0$ in the first Brillouin zone, called the central zone). The mass-weighted Hessian matrix was obtained by numerical differentiation (central-difference formula) of the analytical first energy derivatives, calculated at geometries obtained by displacing, in turn, each of the $3N$ equilibrium nuclear coordinates by a small amount, $u = 0.003$ Å. We refer to a recent work³³ for a complete discussion of the computational conditions and other numerical aspects concerning the calculation of the vibrational frequencies at the Γ point. Using the optimized geometries and the associated vibrational frequencies, CRYSTAL06 computes the total free energy by correcting the electronic energy by the standard statistical thermodynamics formulas based on partition functions derived from the harmonic oscillator approximations.⁴¹

2.2. RIV Coordinates in the CRYSTAL Code and the DRC Strategy. In the DRC method, a proper initial guess for the direct TS search is needed, so that calculations to pass from the reactant domain to the TS domain of the PES are required. This is achieved by enforcing a number of geometrical constraints as detailed below. In this sense, the most critical issues in the computational implementation of the DRC scheme described above involve the definition of (i) suitable constraints into the optimizations at each fixed point along the reaction coordinate and (ii) a suitable coordinate system for the subspace of the remaining degrees of freedom to ensure the best efficiency of the optimization process.

For the first point, the target is to find a single geometrical parameter (at the moment no more than two parameters are allowed in the present CRYSTAL implementation) suitable to represent the reaction coordinate controlling the TS search. This condition is generally satisfied by choosing internal valence coordinates. Indeed, valence parameter sets, i.e., interatomic distances, angles, and dihedrals, are particularly suitable to describe chemical reactions or phase transitions that essentially involve bonding scheme changes.

For molecules, the valence internal parameters are usually defined by means of the Z-matrix approach. Unfortunately, the resulting Z-matrix coordinate system may not be a good choice for structures that exhibit closed connectivity loops, as the Z-matrix scheme suffers from arbitrariness in the definition of the set, causing slow convergence in the optimization procedure.¹ This is indeed in contrast with the request of point ii described above. For infinite structures like crystals, slabs, or polymers, exploiting symmetry equivalences is essential to reduce the complexity of the system (in principle, infinite) to a degree in which it becomes computationally tractable. Unfortunately, the symmetry constraints (even in the $P1$ case, restricted to translational

equivalence) increase dramatically the number of dependencies between internal coordinates, which are formally similar to the closed loops featured by polycyclic molecules, with similar convergence problems. For this reason, the Z-matrix scheme cannot be adopted for geometry optimizations of periodic structures.

A possible solution is to adopt the RIV set of parameters, which allows one to define both the constraints and the coordinate system for the geometry optimization. This coordinate system keeps all the advantages of the valence parameters and additionally reduces the arbitrariness in their definition, allowing a well-balanced description of the structure itself.^{1,3,17} The definition of the RIV sets and their implementation in geometry optimizations of molecules^{1,3} and crystals¹⁷ have already been reported. Accordingly, the details of the methods will not be repeated here, and only the key differences between the present and previous implementations will be highlighted in the present work.

The first step is to define the atomic connectivity (required to define the RIV coordinates) following the recipe of ref 3. Additionally, in the present implementation, all symmetry equivalences within the RIV set are automatically set up so that an irreducible RIV set that consists of one representative of each symmetry class is kept in memory together with its multiplicity per unit cell, μ_i . A small displacement given in the reference coordinate system, $\delta\mathbf{x}$, can be transformed to $\delta\mathbf{q}$ in the RIV basis set, as

$$\delta\mathbf{q} = \mathbf{B}\delta\mathbf{x} \quad (1)$$

where \mathbf{B} is the Wilson \mathbf{B} matrix whose elements read $B_{ij} = \mu_i \partial q_i / \partial x_j$.¹

For periodic systems, it is customary to adopt as the reference coordinate set both the atomic Cartesian coordinates and the Cartesian lattice vectors, in terms of which the gradient is computed by analytic derivation of the energy.¹⁷ Within this approach, both the external and the nontotally symmetric degrees of freedom constitute the redundant set adopted for geometry optimizations. In the present implementation, however, the atomic part of the reference coordinate set envisages a free set of internal and symmetry adapted linear combinations of the atomic fractional coordinates. The lattice part is a complete free set of symmetry-adapted unit cell elastic distortions. This reference set contains an irreducible number of coordinates free from both external and asymmetric displacements. In order to save both memory and computational time in matrix products, the algorithm coded in CRYSTAL always keeps the gradient defined in terms of this nonredundant reference set in the random access memory. Accordingly, in the following, the reference set $\{x_i\}$ always refers to this nonredundant coordinate system.

The \mathbf{B} matrix is computed by numerical differentiation adopting the central point approximation. The force \mathbf{f}_q expressed in RIV coordinates is determined from the force \mathbf{f}_x in the reference system as

$$\mathbf{f}_q = \mathbf{B}^+ \mathbf{f}_x \quad (2)$$

where $f_{q_i} = -\partial E / \partial q_i$ and $\mathbf{B}^+ = \mathbf{G}^+ \mathbf{B}^T$, the superscript “+” indicating generalized inverse and $\mathbf{G} = \mathbf{B}^T \mathbf{B}$.

To carry out optimizations with constraints as required to explore the PES around the TS, the projector onto the subspace common to the nonredundant and free geometrical subspaces is calculated through³

$$\mathbf{P}' = \mathbf{P} - \mathbf{P}\mathbf{C}(\mathbf{C}\mathbf{P}\mathbf{C})^{-1}\mathbf{C}\mathbf{P} \quad (3)$$

where $\mathbf{P} = \mathbf{G}^+ \mathbf{G}$ and \mathbf{C} are the projectors onto the nonredundant and the constraint subspaces, respectively. The latter is given in RIV coordinates as

$$\mathbf{C} \equiv C_{ij} = \begin{cases} 1 & \text{if } i = j \text{ and } i \text{ is constrained} \\ 0 & \text{otherwise} \end{cases} \quad (4)$$

Both the gradient and the Hessian have to be projected out. For the Hessian, the projected matrix $\tilde{\mathbf{H}} = \mathbf{P}'\mathbf{H}\mathbf{P}'$ is diagonalized, and its generalized inverse is computed as

$$[\tilde{H}^{-1}]_{ij} = \sum_k T_{ik} [h_k]^{-1} T_{jk} \quad (5)$$

where T_{ik} is the element of the eigenvectors matrix. By identifying the number of redundant degrees of freedom (difference between the dimensions of the RIV and the free subspaces) as n , the sum over k in eq 5 includes all eigenvalues of $\tilde{\mathbf{H}}$ with the exception of the n ones exhibiting the lowest absolute value. This selection is performed so as to prevent displacements occurring outside the free subspace defined by \mathbf{P}' and to correct for small numerical errors that derive from the numerical evaluation of the \mathbf{B} matrix.

Once the displacements in the RIV coordinate set are computed, a back-transformation to the Cartesian set is carried out in the iterative manner proposed in ref 3. The numerical calculation of the Hessian matrix for the TS optimization is performed in the reference coordinate system, \mathbf{H}_x , in a similar fashion to that considered for the calculation of vibrational modes in CRYSTAL,³³ with the difference that here only the internal totally symmetric displacements are considered. After the construction, the matrix \mathbf{H}_x is transformed to the RIV system according to $\mathbf{H} \equiv \mathbf{H}_q = \mathbf{B}^+ \mathbf{H}_x (\mathbf{B}^+)^T$.

2.3. Modeling of the H-Chabazite Structure. Most of the computational works^{42–48} addressed hitherto to predict proton jump barriers in acidic zeolites were carried out by either cluster or embedded calculations, whereas, to our knowledge, no works at a full ab initio level of periodic calculations are available. The disparity of the computed energy barriers (spanning the 12–35 kcal mol^{−1} range, in absence of water) is mainly due to the different methodologies and approaches adopted to model the acidic zeolites. The simplest is based on the cluster approach, which consists of extracting from the infinite solid a finite cluster surrounding the active site. For small clusters, full ab initio calculations have been carried out, whereas for larger clusters, the ONIOM strategy⁴⁹ has been adopted. In the latter, the whole systems are divided into different layers, each one being treated at different computational levels: the active site at the highest level of theory, with the rest at the lowest one. Irrespective of these differences, in both procedures, zeolites were treated by means of standard molecular quantum methods so that the lack of long-range effects may cause various pitfalls.⁵⁰ The inclusion of long-range effects needs the treatment of the whole solid systems (namely, zeolites

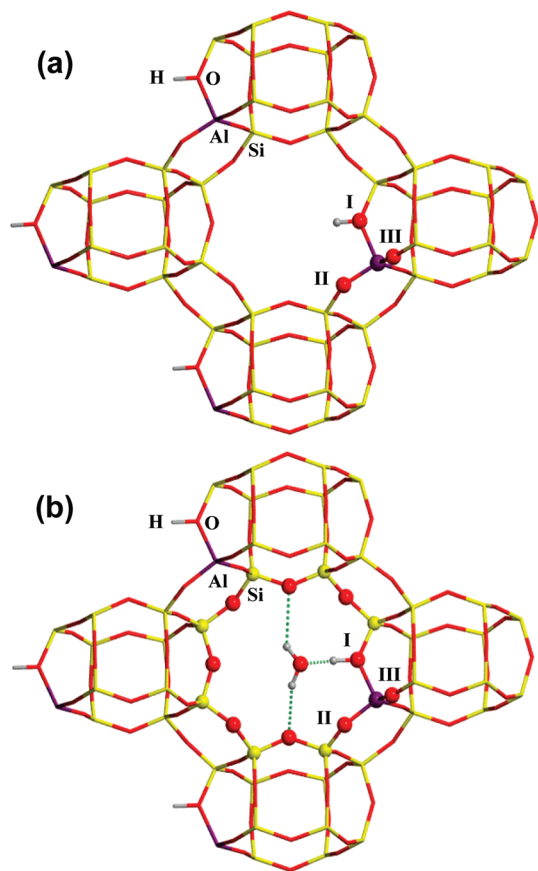


Figure 1. H-CHA periodic model used to study the proton jump between sites I, II, and III. Sections: (a) dry H-CHA; (b) H-CHA plus one H₂O molecule.

as infinite solids) via a periodic approach. In the past, periodicity has been exploited either (i) via embedding techniques, such as the QM-Pot method,⁵¹ which partitions the periodic system into two parts, the inner zone, containing the reaction site and treated by quantum mechanics, and the outer zone, described by a properly parametrized classical interatomic potential, and (ii) via full ab initio periodic calculations, ensuring that both the local properties and the long-range effects are treated with the same accuracy. Critical points for the embedding approaches are the absence of charge flux between the inner and outer zones and the difficulty to derive proper interatomic potentials, especially when modeling chemical reactions, whereas the advantage is the freedom to adopt for the inner zone highly accurate quantum mechanical levels (i.e., MP2, CCSD(T), ...), which are not generally available in a fully periodic approach. The latter offers, however, a very clean approach completely free from the previous pitfalls at the expense of being somehow limited to density functional theory as the best level of theory. Some relevant progress has, however, recently been achieved in that respect, as the CRYSCOR program, starting from the Hartree-Fock solution provided by CRYSTAL, can refine the total energy of the crystal at the MP2 level, although at present, it is limited to single point energy evaluation.^{52,53}

Considering the above points, in the present work, a periodic model for the H-chabazite has been adopted (shown in Figure 1). It arises from the structure of the pure silica chabazite (CHA),⁵⁴ which consists of a network of double

six-membered silica rings (hexagonal prisms) connected by four-membered rings. By adopting a Si/Al ratio of 11:1 (one aluminum atom per unit cell), the symmetry of all-silica CHA is reduced from the $R\bar{3}m$ to the $P1$ space group. Charge compensation is achieved by the addition of a proton to one of the four oxygen atoms of the AlO_4 tetrahedron (H-CHA). The resulting unit cell (37 atoms) has $\text{HAlSi}_{11}\text{O}_{24}$ as its chemical formula. The four H-CHA structures exhibit different stabilities, the most favored one corresponding to the proton attached to site I (see Figure 1a).⁵⁵ It is well-known that proton jumps from one oxygen to the others may occur, so that the implementation of the DRC method has been tested by computing the energy profile for the proton jumps in H-CHA following the $\text{I} \rightarrow \text{II} \rightarrow \text{III} \rightarrow \text{I}$ path (see Figure 1a).⁴⁷ For each step, full characterization of minima and the TS has been achieved. Furthermore, the same proton jump route has also been characterized in the presence of one water molecule that acts as a proton transfer helper. Indeed, traces of water in the H-CHA have been demonstrated to significantly reduce the energy barriers.^{48,56} For this latter case, the most stable H-CHA/H₂O complex consists of the acidic proton attached to site I engaged in rather strong H-bonds with the H₂O molecule (see Figure 1b).⁵⁰

3. Results and Discussion

3.1. Proton Jump Path $\text{I} \rightarrow \text{II}$ with the B3LYP Hamiltonian. The need to maximize the energy in one (and only one) direction to locate the saddle point on a PES is a very delicate process because too rough TS structures will not converge to the proper final TS. The DRC technique approaches the TS search in two successive steps: (i) defining a structure as close as possible to the TS and (ii) refining this structure to exactly locate the actual TS. As described in the Computational Details section, the present DRC scheme optimizes both the atomic and cell parameters during the search for a TS, at variance with the usual CI-NEB technique in which, despite some recent modifications,¹¹ the cell part is always kept fixed. In the following, this procedure is described in detail.

Defining a Geometry Close to the TS. A geometry close to the TS is defined by a scan calculation along any internal coordinate that may govern the reaction. This scan calculation consists in evolving, step by step and in a controlled way, the selected internal coordinate so as to move from reactants to products by crossing a point of maximum energy. For instance, the proton jump from site I to II implies the breaking and the formation of the O1-H and H-O2 bonds (see Figure 1a), respectively, so that the $\text{H}\cdots\text{O2}$ distance may be considered as the internal coordinate that drives the reaction (the so-called reaction coordinate). The scan calculation, based on the $\text{H}\cdots\text{O2}$ distance, evolves from the reactant geometry toward the product in many steps along the reaction coordinate; namely, the $\text{H}\cdots\text{O2}$ distance shortens from reactants toward products. At each step, the value of the reaction coordinate is frozen while all other internal coordinates are relaxed, so that a “pseudo-optimized” structure is computed. At the end of the scan calculation, a set of

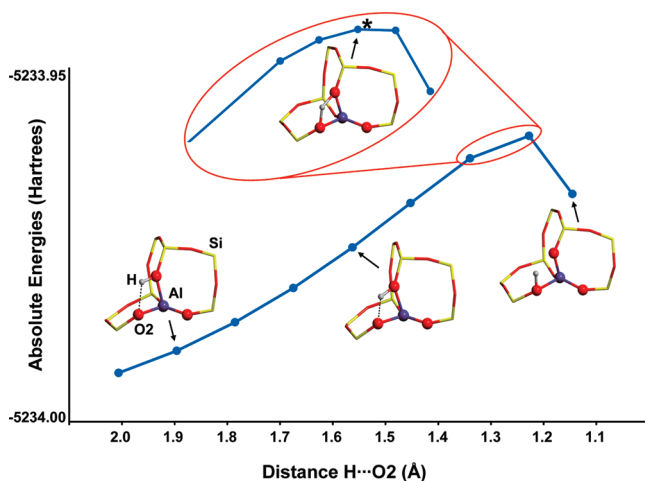


Figure 2. Electronic energy variation during the scan process. The H...O2 distance (restricted reaction coordinate) is frozen at different values, while the remaining internal coordinates are optimized. The red inset zone shows a finer scan with smaller steps close to the energy maximum. The asterisk marks the structure used as the initial guess for the final TS search.

intermediate energy points connecting reactants and products (defined by the various partially optimized structures) is arrived at. Focusing on the present case, the H...O2 distance is scanned from an initial value of 2.0 Å to a final value of 1.1 Å, with 9 partially optimized structures, each differing by a step of -0.1 Å. The energy variation as a function of the DRC is shown in Figure 2. This “distinguished energy profile” exhibits three different zones: (i) a zone where the energy rises moderately as the H...O2 distance shortens (reactant-like zone, the H–O1 bond has not yet been broken), (ii) a zone where the energy is rather high and goes through a maximum (TS-like zone, the proton is almost midway between O1 and O2 positions), and (iii) a zone where the energy decreases (product-like zone, the proton is already bound to O2). The structure at the energy maximum is therefore used to define the initial guess for the next step, i.e., the accurate TS geometry localization. Although not mandatory, a second scan calculation with smaller steps (see inset of Figure 2) around the maximum energy zone (i.e., between 1.3 and 1.2 Å) can be carried out in order to refine the geometry used to secure the initial guess for the TS search.

Geometry Optimization to a TS. Starting from the above structure within the TS domain, the Hessian matrix is then computed, either via numerical estimate (very accurate but expensive) or through empirical models (cheaper but less accurate), to ensure that the algorithm will follow the right direction toward the final TS. Irrespective of the way to compute the Hessian matrix, the SCF energy tolerance must however be tightened to 10^{-10} to 10^{-11} Hartree in order to reach the needed numerical accuracy.

Adopting the above scheme, the TS for the proton transfer from site I to site II has been easily located. In the optimized TS, the H–O2 distance is 1.245 Å, which lies almost between the value for the maximum energy structure (1.26 Å) and the next structure (1.24 Å) in the scan calculation. It is worth mentioning that the same TS structure was arrived

at irrespective of the initial guesses which may result from a search based on either a coarse (0.1 Å) or a finer step size (0.02 Å), although for the latter, less optimization cycles are needed to locate the TS. Further details related to the keywords needed to setup both the scan calculation and the TS search are provided in the Supporting Information (SI) as complete CRYSTAL input files.

3.2. Proton Jump Path I \rightarrow II with Different Hamiltonians. To study the dependence of the TS features on the adopted Hamiltonian, the proton jump from site I to II has been computed at HF, PW91, PBE, PBE0, and B3LYP using the same Gaussian basis set reported in the Computational Details section. The structural parameters of the optimized stationary points are reported in Table 1, whereas the reaction energies (ΔE_r) and energy barriers (ΔE^\ddagger) are shown in Table 2. Within the same basis set, the computed ΔE_r values are all rather close to each other as a function of the adopted method, the highest value being for HF (3.3 kcal mol $^{-1}$) compared to density functional values ($\Delta E_r = 1.3$ –2.2 kcal mol $^{-1}$). Similarly, the DF energy barriers, ΔE^\ddagger , computed with different DF methods are also very close to each other, lying within a window of 13.6–15.0 kcal mol $^{-1}$, but for that computed at the HF level, which is as high as 30.2 kcal mol $^{-1}$. These values are consistent with the performance of the considered methods in describing proton transfer reactions:⁵⁷ the lack of electron correlation in HF yields a dramatic overestimation of the energy barrier, whereas the balanced electron exchange-correlation included in the definition of the DF methods leads to similar ΔE^\ddagger values. The O2–H distances and transition frequency (ν^\ddagger) of the TS structures are also dependent on the adopted method, HF systematically providing a too short O2–H distance (1.217 Å) and a too high ν^\ddagger (1801 cm $^{-1}$) compared to the DF methods (O2–H distances lying between 1.233 and 1.245 Å, ν^\ddagger lying between 1085 and 1218 cm $^{-1}$). As quoted in the Introduction, an important issue of the present implementation is its ability to locate the TS by including also the relaxation of the cell parameters. To understand the role that cell parameter relaxation has on the energy barriers, the proton jump has been computed with both PBE and B3LYP functionals by keeping the cell parameters fixed to the values optimized for the reactants. The values reported in Table 2 (“fixed cell” label) show that fixing the cell parameters, while not affecting the thermodynamics (ΔE_r values), increases the energy barriers ΔE^\ddagger by about 3–4 kcal mol $^{-1}$, reducing the reaction speed by almost 3 orders of magnitude. Accordingly, the ν^\ddagger values for the “fixed cell” cases are all definitely higher than those computed with relaxed cell parameters. Considering that the present TSs involve relatively small molecular aggregates, these results emphasized the relevance of cell relaxation, which will become clearly mandatory for reactions involving bulky reactants.

A comparison of the present results with previous studies allows one to assess whether the actual DRC strategy provides similar potential energy surface features. The closest theoretical work to the present study is the one by Sierka and Sauer,⁴⁷ in which the proton jump I \rightarrow II in the H–CHA was computed by the QM-Pot method, treating the quantum

Table 1. Selected Distances (Å) of the Structures Involved in the Proton Jump from Site I to II, Computed with Different Methods

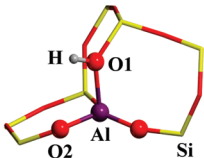
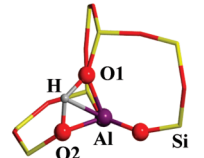
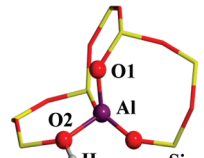
Structure	Distance	HF	PW91-PW91	PBE-PBE	PBE0	B3LYP	B3LYP triple- ζ
	O1-H	0.949	0.976	0.977	0.966	0.969	0.966
	O2-H	2.591	2.577	2.576	2.576	2.565	2.563
	O1-Al	1.906	1.900	1.904	1.892	1.899	1.912
	O2-Al	1.692	1.710	1.712	1.700	1.703	1.704
	O1-H	1.227	1.251	1.250	1.210	1.222	1.233
	O2-H	1.217	1.233	1.237	1.238	1.245	1.239
	O1-Al	1.791	1.808	1.812	1.826	1.830	1.837
	O2-Al	1.802	1.816	1.819	1.816	1.820	1.825
	O1-H	3.357	3.438	3.441	3.408	3.398	3.350
	O2-H	0.951	0.978	0.978	0.968	0.971	0.968
	O1-Al	1.876	1.714	1.717	1.703	1.877	1.708
	O2-Al	1.696	1.883	1.886	1.873	1.705	1.876

Table 2. Electronic Energy Barriers and Reaction Energies, ΔE^\ddagger and ΔE_r (kcal mol⁻¹) for the Proton Jump from Site I to II, Computed with Different Methods^a

	ΔE^\ddagger	ΔE_r	ν^\ddagger
HF	30.2	3.3	1801 <i>i</i>
PW91-PW91	14.5	1.5	1089 <i>i</i>
PBE-PBE	14.4	1.3	1085 <i>i</i>
PBE-PBE (fixed cell)	18.4	1.6	1273 <i>i</i>
PBE0	13.6	2.1	1129 <i>i</i>
B3LYP	15.0	2.2	1218 <i>i</i>
B3LYP (fixed cell)	18.3	2.6	1334 <i>i</i>
B3LYP/triple- ζ	17.1	3.5	1308 <i>i</i>
QM-Pot(B3LYP/T(O)DZP:EVP) ^b	17.6	2.1	1151 <i>i</i>

^a Values of proton jump transition frequencies, ν^\ddagger (cm⁻¹), are also included. ^b EVP refers to empirical valence bond adopted for the outer zone, see ref 21.

mechanical region at the B3LYP level combining an Ahlrich's Gaussian double- ζ polarized basis set, for H, Si, and Al, and a triple- ζ polarized for O (T(O)DZP). Their energy barrier for the proton jump resulted in 17.6 kcal mol⁻¹, 2.6 kcal mol⁻¹ higher than the one computed here. To decrease the inconsistency between our standard basis set and that adopted by Sierka and Sauer, the whole DRC was recomputed with the larger basis set described in the Computational Details section (a triple- ζ polarized quality Gaussian basis set) resulting in a $\Delta E^\ddagger = 17.1$ kcal mol⁻¹, in almost perfect agreement with the value computed by Sierka and Sauer. It is worth noting, however, that whereas the DRC calculations include cell parameter relaxation along the considered points of the potential energy surface, the QM-pot calculations were

carried out at fixed cell parameters, causing some inconsistency in the comparison.

3.3. Proton Jumps in Dry and Wet Conditions. In this section, the DRC has been adopted to study the proton jump in H-CHA, either in dry conditions or in the presence of one water molecule acting as a proton jump helper. For both cases, the acidic H attached to O1 is the most stable site, and the proton jump has been studied along the following path: I \rightarrow II \rightarrow III \rightarrow I. The computed B3LYP-energy profiles as well as the stationary points are shown in Figures 3 and 4, for the dry and wet cases, respectively.

The intrinsic order of stability (namely, without solvent) of the different AlO₄ Brønsted sites resulted in the following order (considering free energies at $T = 298$ K): O1 > O3 > O2. This sequence is identical to those obtained both at the QM-Pot level⁴⁷ as well as through full periodic pseudopotential plane-wave calculations.⁵⁸ Additionally, experimental measurements revealed that protonation occurs only at sites I and III⁵⁹ (note the different numbering of oxygen sites in ref 59), so that our results are consistent with previous data.

In the absence of water, the I \rightarrow II process has the lowest energy barrier ($\Delta E^\ddagger = 15.0$ kcal mol⁻¹), whereas the II \rightarrow III and III \rightarrow I ones exhibit higher barriers (around 19 kcal mol⁻¹). This trend is unchanged also when free energies are considered, albeit the energy barriers are lowered by 4 kcal mol⁻¹. The present value of 18.7 kcal mol⁻¹ for the ΔE^\ddagger associated to the III \rightarrow I path is in good agreement with the value of 20.5 kcal mol⁻¹ computed by Sierka and Sauer, considering that different basis sets have been used (see the

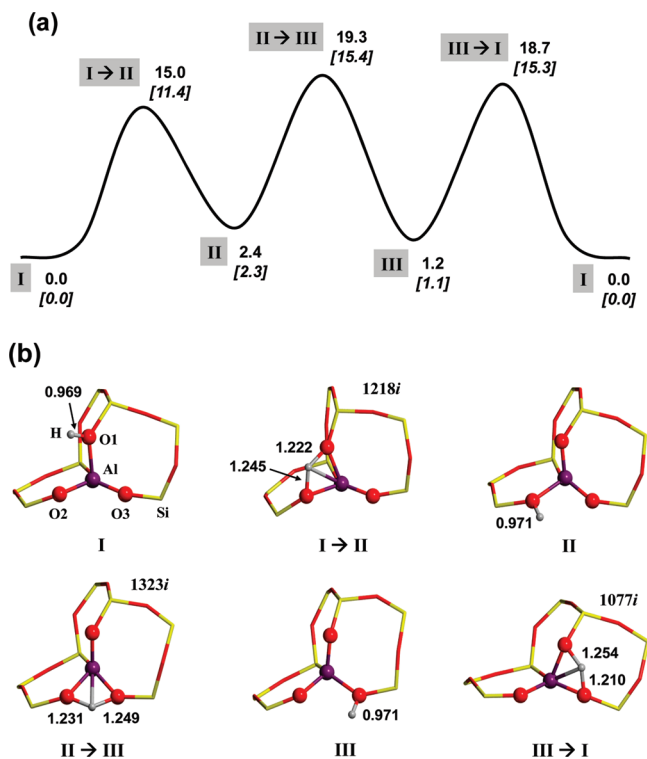


Figure 3. (a) B3LYP-energy profile of the proton jump along the $I \rightarrow II \rightarrow III \rightarrow I$ path in dry conditions. Bare values as relative electronic energies, values in brackets as relative free energies at $T = 298$ K with respect to the proton at site I. (b) B3LYP-optimized structures corresponding to stationary points in the energy profile of section a. Bond distances in Å, energies in kcal mol^{-1} .

previous discussion for the $I \rightarrow II$ path). Free cluster calculations reported by Sauer et al.⁶⁰ gave $\Delta E^\ddagger = 12$ kcal mol^{-1} , which is considerably lower than the full periodic B3LYP value. The underestimation of the energy barriers provided by free cluster models compared to more constrained systems was already noticed in a comprehensive study by Fermann et al.,⁴⁵ in which results of the proton jumps occurring in H-Y zeolites simulated by free and embedded clusters were compared.

The presence of one water molecule does cause a significant lowering of the energy barriers, indeed acting as a proton helper. Considering only free energies, energy barriers for $I \rightarrow II$ and $II \rightarrow III$ paths decrease by 8–10 kcal mol^{-1} , whereas for the $III \rightarrow I$ path, the lowering is only by 4 kcal mol^{-1} . These results confirm that, in H-CHA zeolites, the presence of water, even at trace levels, will dramatically alter the proton mobility. The mechanism of proton jump assistance was already observed in zeolites not only for water but also in the presence of other protic solvents, such as methanol and ethanol.⁴⁶

Large differences for the two cases in the ν^\ddagger values have also been predicted: for the water-free H-CHA, the ν^\ddagger value was about 1000 cm^{-1} , which reduces to around 200 cm^{-1} (see Figures 3b and 4b, respectively) when water is assisting the proton jump. These values are consistent with the higher geometrical strain (four-membered ring) present in the water-free TS structures compared to the six-membered ring in the presence of one water molecule.

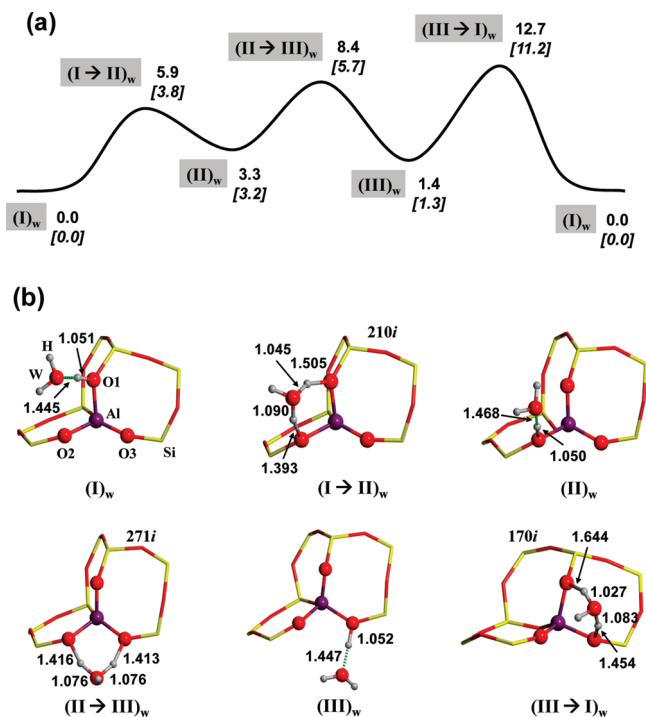


Figure 4. (a) B3LYP-energy profile of the proton jump along the $I \rightarrow II \rightarrow III \rightarrow I$ path in the presence of one H_2O molecule acting as a proton transfer helper. Bare values as relative electronic energies, values in brackets as relative free energies at $T = 298$ K with respect to the proton at site I. (b) B3LYP-optimized structures corresponding to stationary points in the energy profile of section a. Bond distances in Å, energies in kcal mol^{-1} .

Tuma and Sauer⁴⁸ computed the proton jump in H-CHA from site II to III (please note the different numbering scheme of oxygen sites adopted in ref 48) within a QM/QM approach (PBE functional as a lower method, MP2 method as a high-level one). This MP2/DFT scheme gave the proton jump energy barrier of 6.2 kcal mol^{-1} with an Ahlrich's triple- ζ basis set for O atoms and double- ζ basis set for the remaining elements. Our own value with the DRC method gives 5.1 kcal mol^{-1} (considering site II as the reference energy asymptote for consistency with ref 48), in good agreement with Tuma and Sauer's value (for basis set effects, see the above discussion). Finally, from the experimental side, ^1H NMR measurements devoted to the proton exchange rate of different hydrated cation-exchanged (Li, Na, K) CHA allow one to arrive at activation energies (E_a) in the range of 10–14 kcal mol^{-1} .⁶¹ A direct comparison between our computed barriers and those from the experiment is not straightforward considering the ideality of the adopted model (H-CHA with one H_2O molecule) in contrast to a cation-exchanged CHA with relatively high water loading used in the experiment, and thus the relevance of the comparison should be judged with some extra caution. Our closest result to the experimental results corresponds to the direct proton jump from site I to III ($\Delta E^\ddagger = 12.7$ kcal mol^{-1}). Nevertheless, a lower barrier (8.4 kcal mol^{-1}) is possible via the $I \rightarrow II \rightarrow III$ path: notwithstanding, the population of site II will be about 10^{-3} times smaller than that of I, so that experimental barriers may presumably derive from both paths.

4. Conclusions

The automatic scan of valence coordinates has been implemented in the CRYSTAL *ab initio* periodic code as a strategy to search and refine saddle point structures, through the DRC strategy. In order to have a consistent coordinate set of valence parameters for periodic systems, the redundant scheme has been adopted.

The performance of the algorithm has been illustrated for the acidic chabazite (H-CHA) zeolite by considering the jump of the acidic proton between different oxygen atoms of the AlO_4 tetrahedron. It has been shown that, despite the complexity in the connectivity of the atoms that makes the study of the reactions very difficult when considering Cartesian coordinates, the exploration of the PES around the TS becomes straightforward in terms of valence coordinates, hence allowing the use of quite simple strategies such as the DRC one.

Calculations have been carried out for the proton jump between site I and site II with different Hamiltonians, namely, Hartree-Fock, PBE, PW91, PBE0, and B3LYP hybrid functionals with a double- ζ polarized basis set. As expected, Hartree-Fock overestimates the energy barrier and the transition frequency ($\Delta E^\ddagger = 30.2 \text{ kcal mol}^{-1}$ and $\nu^\ddagger = 1801 \text{ cm}^{-1}$, respectively) compared to density functional methods ($\Delta E^\ddagger = 13.6\text{--}15.0 \text{ kcal mol}^{-1}$ and $\nu^\ddagger = 1085\text{--}1218 \text{ cm}^{-1}$, respectively). It is also shown that cell relaxation during the TS localization significantly influences the accuracy of the results, since barriers to proton jumps computed with fixed cell parameters are by 3–4 kcal mol^{-1} higher than those computed with fully relaxed geometry.

A complete proton jump path, $\text{I} \rightarrow \text{II} \rightarrow \text{III} \rightarrow \text{I}$, has been studied, both in the absence and in the presence of one water molecule which assists the proton jump. Proton jumps in water-free H-CHA exhibit higher energy barriers (among 4–10 kcal mol^{-1}) than those computed in the presence of one water molecule, confirming the role of water as a “proton transfer helper”. The free energies of all stationary points have been computed at $T = 298 \text{ K}$ by using the accurate harmonic frequency values provided by the CRYSTAL code, showing values of the free energy barriers somehow lower by 4 kcal mol^{-1} than the purely electronic ones. The accuracy of the present periodic approach to optimize TS structures has been assessed by comparing the electronic energy barriers with those reported in previous theoretical works as well as with the available experimental data, mostly showing very good agreement.

Accordingly, with the present tool, very detailed information of TS structures and free energies can be computed at a reasonable computational cost. The present strategy, moreover, allows one to search for TS structures involving changes in both atomic as well as cell parameters in a very natural way. Relaxing cell parameters may be relevant even for studying localized chemical reactions occurring on adsorbed bulky molecules in zeolite channels, in which expansion or contraction of the silica framework can affect the energy barrier, particularly when dispersive contributions are taken into account.⁶² Obviously, this feature is also mandatory for studying phase transition processes, a point which is under investigation in our laboratory. Other issues

that deserve further studies concern the implementation of a CI-NEB scheme formulated in terms of RIV coordinates.

Acknowledgment. A.R. is indebted to Fundación Ramón Areces for a postdoctoral fellowship. P.U. acknowledges CINECA supercomputing center for a generous allowance of computing time.

Supporting Information Available: Input for a scan calculation and input for a TS search calculation. This material is available free of charge via the Internet at <http://pubs.acs.org>.

References

- (1) Pulay, P.; Fogarasi, G. *J. Chem. Phys.* **1992**, *96*, 2856–2860.
- (2) Peng, C.; Schlegel, H. B. *Israel J. Chem.* **1993**, *33*, 449–454.
- (3) Peng, C.; Ayala, P. Y.; Schlegel, H. B.; Frisch, M. J. *J. Comput. Chem.* **1996**, *17*, 49–56.
- (4) Bell, S.; Crighton, J. S. *J. Chem. Phys.* **1984**, *80*, 2464–2475.
- (5) Fischer, S.; Karplus, M. *Chem. Phys. Lett.* **1992**, *194*, 252–261.
- (6) Halgren, T. A.; Lipscomb, W. N. *Chem. Phys. Lett.* **1977**, *49*, 225–232.
- (7) Hratchian, H. P.; Schlegel, H. B. In *Theory and Applications of Computational Chemistry: The First Forty Years*; Dykstra, C. E., Ed.; Elsevier B. V.: Amsterdam, 2005, pp 195–249.
- (8) Schlegel, H. B. *J. Comput. Chem.* **2003**, *24*, 1514–1527.
- (9) Sholl, D. S.; Steckel, J. A. *Density Functional Theory: A Practical Introduction*; John Wiley & Sons, Inc.: Hoboken, NJ, 2009.
- (10) Henkelman, G.; Uberuaga, B. P.; Jónsson, H. *J. Chem. Phys.* **2000**, *113*, 9901–9904.
- (11) Caspersen, K. J.; Carter, E. A. *Proc. Natl. Acad. Sci.* **2005**, *102*, 6738–6743.
- (12) Press, W. H.; Teukolsky, S. A.; Vetterling, W. T.; Flannery, B. P. *Numerical Recipes*, 3rd ed.; Cambridge University Press: New York, 2007.
- (13) Hennig, R. G.; Trinkle, D. R.; Bouchet, J.; Srinivasan, S. G.; Albers, R. C.; Wilkins, J. W. *Nat. Mater.* **2005**, *4*, 129–133.
- (14) Trinkle, D. R.; Hennig, R. G.; Srinivasan, S. G.; Hatch, D. M.; Jones, M. D.; Stokes, H. T.; Albers, R. C.; Wilkins, J. W. *Phys. Rev. Lett.* **2003**, *91*, 025701.
- (15) Thomas, J. M.; Thomas, W. J. *Principles and Practice of Heterogeneous Catalysis*; Wiley VCH: Weinheim, Germany, 1996.
- (16) Derouane, E. G. *J. Mol. Catal. A: Chem.* **1998**, *134*, 29–45.
- (17) Kudin, K. N.; Scuseria, G. E.; Schlegel, H. B. *J. Chem. Phys.* **2001**, *114*, 2919–2923.
- (18) Rothman, M. J.; Lohr, J. L.; Ewig, C. S.; Wazer, J. R. V. In *Potential Energy Surfaces and Dynamical Calculations*; Truhlar, D. G., Ed.; Plenum: New York, 1979, pp 653–660.
- (19) Dovesi, R.; Saunders, V. R.; Roetti, C.; Orlando, R.; Zicovich-Wilson, C. M.; Pascale, F.; Civalleri, B.; Doll, K.; Harrison, N. M.; Bush, I. J.; D’Arco, P.; Llunell, M. *CRYSTAL06 User’s Manual*; University of Torino: Torino, Italy, 2006.

- (20) Auerbach, S. M.; Carrado, K. A.; Dutta, P. K. In *Handbook of Zeolite Science and Technology*; Marcel Dekker: New York, 2003.
- (21) Corma, A. *Chem. Rev.* **1995**, *95*, 559–614.
- (22) Huber, G. W.; Iborra, S.; Corma, A. *Chem. Rev.* **2006**, *106*, 4044–4098.
- (23) Meusinger, J.; Corma, A. *J. Catal.* **1996**, *159*, 353–360.
- (24) Sauer, J.; Ugliengo, P.; Garrone, E.; Saunders, V. R. *Chem. Rev.* **1994**, *94*, 2095–2160.
- (25) Kwan, S. M.; Yeung, K. L. *Chem. Commun.* **2008**, 3631–3633.
- (26) Perdew, J. P.; Burke, K.; Ernzerhof, M. *Phys. Rev. Lett.* **1996**, *77*, 3865–3868.
- (27) Perdew, J. P.; Chevary, J. A.; Vosko, S. H.; Jackson, K. A.; Pederson, M. R.; Singh, D. J.; Fiolhais, C. *Phys. Rev. B* **1992**, *46*, 6671–6687.
- (28) Adamo, C.; Barone, V. *J. Chem. Phys.* **1999**, *110*, 6158–6170.
- (29) Becke, A. D. *J. Chem. Phys.* **1993**, *98*, 5648–5652.
- (30) Lee, C.; Yang, W.; Parr, R. G. *Phys. Rev. B* **1988**, *37*, 785–789.
- (31) http://www.crystal.unito.it/Basis_Sets/Ptable.html (accessed Mar 2010).
- (32) Monkhorst, H. J.; Pack, J. D. *Phys. Rev. B* **1976**, *8*, 5188–5192.
- (33) Pascale, F.; Zicovich-Wilson, C. M.; Gejo, F. L.; Civalleri, B.; Orlando, R.; Dovesi, R. *J. Comput. Chem.* **2004**, *25*, 888–897.
- (34) Pascale, F.; Tosoni, S.; Zicovich-Wilson, C.; Ugliengo, P.; Orlando, R.; Dovesi, R. *Chem. Phys. Lett.* **2004**, *396*, 308–315.
- (35) Schlegel, H. B. *J. Comput. Chem.* **1982**, *3*, 214–218.
- (36) Simons, J.; Nichols, J. *Int. J. Quantum Chem. Quantum Chem. Symp.* **1990**, *24*, 263–276.
- (37) Murtagh, B. A.; Sargent, R. W. H. *Comput. J.* **1970**, *13*, 185–194.
- (38) Bofill, J. M. *J. Comput. Chem.* **1994**, *15*, 1–11.
- (39) Binkley, J. S.; Whiteside, R. A.; Krishnan, R.; Seeger, R.; Defrees, D. J.; Schlegel, H. B.; Topiol, S.; Kahn, L. R.; Pople, J. A. *Gaussian 80*; Carnegie-Mellon Quantum Chemistry Publishing Unit: Pittsburgh, PA, 1980.
- (40) Civalleri, B.; D’Arco, P.; Orlando, R.; Saunders, V. R.; Dovesi, R. *Chem. Phys. Lett.* **2001**, *348*, 131–138.
- (41) McQuarrie, D. *Statistical Mechanics*; Harper and Row: New York, 1986.
- (42) Fermann, J. T.; Auerbach, S. *J. Chem. Phys.* **2000**, *112*, 6787–6794.
- (43) Fermann, J. T.; Blanco, C.; Auerbach, S. *J. Chem. Phys.* **2000**, *112*, 6779–6786.
- (44) Sierka, M.; Sauer, J. *J. Chem. Phys.* **2000**, *112*, 6983–6996.
- (45) Fermann, J. T.; Moniz, T.; Kiowski, O.; McIntire, T. J.; Auerbach, S. M.; Vreven, T.; Frisch, M. J. *J. Chem. Theory Comput.* **2005**, *1*, 1232–1239.
- (46) Ryder, J. A.; Chakraborty, A. K.; Bell, A. T. *J. Phys. Chem. B* **2000**, *104*, 6998–7011.
- (47) Sierka, M.; Sauer, J. *J. Phys. Chem. B* **2001**, *105*, 1603–1613.
- (48) Tuma, C.; Sauer, J. *Chem. Phys. Lett.* **2004**, *387*, 388–394.
- (49) Dapprich, S.; Komáromi, I.; Byun, K. S.; Morokuma, K.; Frisch, M. J. *THEOCHEM* **1999**, *461–462*, 1–21.
- (50) Solans-Monfort, X.; Sodupe, M.; Branchadell, V.; Sauer, J.; Orlando, R.; Ugliengo, P. *J. Phys. Chem. B* **2005**, *109*, 3539–3545.
- (51) Sauer, J.; Sierka, M. *J. Comput. Chem.* **2000**, *21*, 1470–1493.
- (52) Maschio, L.; Usvyat, D.; Manby, F. R.; Casassa, S.; Pisani, C.; Schutz, M. *Phys. Rev. B* **2007**, *76*, 075101.
- (53) Pisani, C.; Maschio, L.; Casassa, S.; Halo, M.; Schutz, M.; Usvyat, D. *J. Comput. Chem.* **2008**, *29*, 2113–2124.
- (54) Díaz-Cabañas, M.-J.; Barrett, P. A. *Chem. Commun.* **1998**, 1881–1882.
- (55) Civalleri, B.; Ferrari, A. M.; Llunell, M.; Orlando, R.; Merawa, M.; Ugliengo, P. *Chem. Mater.* **2003**, *15*, 3996–4004.
- (56) Chalk, A. J.; Radom, L. *J. Am. Chem. Soc.* **1997**, *119*, 7573–7578.
- (57) Koch, W.; Holthausen, M. C. *A Chemist’s Guide to Density Functional Theory*; Wiley-VCH: Weinheim, Germany, 2000.
- (58) Jeanvoine, Y.; Ángyán, J. G.; Kresse, G.; Hafner, J. *J. Phys. Chem. B* **1998**, *102*, 5573–5580.
- (59) Smith, L. J.; Davidson, A.; Cheetham, A. K. *Catal. Lett.* **1997**, *49*, 143–146.
- (60) Sauer, J.; Kölmel, C. M.; Hill, J.-R.; Ahlrichs, R. *Chem. Phys. Lett.* **1989**, *164*, 193–198.
- (61) Afanassyev, I. S.; Moroz, N. K.; Belitsky, I. A. *J. Phys. Chem. B* **2000**, *104*, 6804–6808.
- (62) Tuma, C.; Sauer, J. *Phys. Chem. Chem. Phys.* **2006**, *8*, 3955–3965.

CT900680F